

₁ Physics-Infused Reduced-Order Modeling for Analysis of
₂ Ablating Hypersonic Thermal Protection Systems

₃

₄ November 11, 2025

₅ **Abstract**

This work presents a *physics-infused reduced-order modeling* (PIROM) framework towards the design, analysis, and optimization of non-decomposing ablating hypersonic thermal protection systems (TPS). It is demonstrated via the modeling of transient thermo-ablative behavior of non-decomposing multi-layered hypersonic TPS. The PIROM architecture integrates a reduced-physics backbone, based on the lumped-capacitance model (LCM), with data-driven correction dynamics formulated via a coarse-graining approach rooted in the Mori-Zwanzig formalism. The LCM is coupled to a surface velocity model (SVM) to capture the recession of the ablating TPS as a function of the surface temperature. While the LCM and SVM capture the dominant physics of the ablating TPS response, the correction terms compensate for residual dynamics arising from higher-order non-linear interactions and heterogeneities across material layers. The PIROM consistently achieves errors below 1% for a wide range of extrapolative settings of design parameters involving time-and-space varying boundary conditions and SVM models, and improves by $x\%$ over the LCM alone. Moreover, the PIROM delivers online evaluations that are two orders of magnitude faster than the full-order model (FOM). These results demonstrate that PIRO effectively reconciles the trade-offs between accuracy, generalizability, and efficiency, providing a promising framework for optimizing multi-physical dynamical systems, such as TPS under diverse operating conditions.

₂₅ **1 Introduction**

₂₆ At hypersonic speeds, aerospace vehicles experience extreme aero-thermo-dynamic environments that require specialized thermal protection systems (TPS) to shield internal sub-
₂₇ structures, electronics, and possibly crew members from the intense aerodynamic heating.
₂₈

29 The TPS is often composed of ablating materials – a high-temperature capable fibrous
30 material injected with a resin that fills the pore network and strengthens the composite
31 [Amar2016](#). The TPS design promotes the exchange of mass through thermal and
32 chemical reactions (i.e., pyrolysis), effectively mitigating heat transfer to the sub-structures.

33 As a result, accurate prediction for the ablating TPS response under extreme hyper-
34 sonic heating becomes fundamental to ensuring survivability, performance, and safety of
35 hypersonic vehicles. Not only is it necessary to assess the performance of the thermal man-
36 agement systems, but also the shape changes of the vehicle’s outer surface induced by the
37 ablating material, and its impact on the aerodynamics, structural integrity, and controlla-
38 bility. Nonetheless, high-fidelity simulations of ablating TPS remains a formidable challenge
39 both theoretically and computationally.

40 Unfortunately, high-fidelity simulations of ablating TPS remains a formidable challenge
41 both theoretically and computationally.

42 On the theoretical side, the thermo-chemical reactions, coupled with the irregular pore
43 network structure, translate into simplifying assumptions to reduce non-linearities, and make
44 the resulting equations more amenable for engineering application and design analysis [x](#).
45 For instance, one of the most notable codes is the one-dimensional [CMA](#) code that was
46 developed by Aerotherm Corporation in the 1960s [Howard2015](#). Despite its practical use
47 in...

48 Another example is the CHarring Ablator Response (CHAR) ablation code, which ignores
49 elemental decompositions of the pyrolyzing gases, assumes the gases to be a mixture of perfect
50 gases in thermal equilibrium, and assumes no reaction or condensation with the porous
51 network [?].

52 [theoretically:](#)

53 [computationally:](#)

54 2 Modeling of Ablating Thermal Protection Systems

55 This section presents the problem of modeling a non-decomposing ablating TPS subjected to
56 extreme hypersonic heating. Two different but mathematically connected solution strategies
57 are provided: (1) a high-fidelity full-order model (FOM) based on a finite element method
58 (FEM), and (2) a low-fidelity reduced-physics model (RPM) based on a lumped capacitance
59 model (LCM) and a one-dimensional surface velocity model (SVM). The FOM is compu-
60 tationally expensive but provides the highest fidelity, while the RPM is computationally
61 efficient but has low predictive fidelity; both models are amenable to high-dimensional de-
62 sign variables. The RPM is used in the subsequent sections for deriving the PIROM.

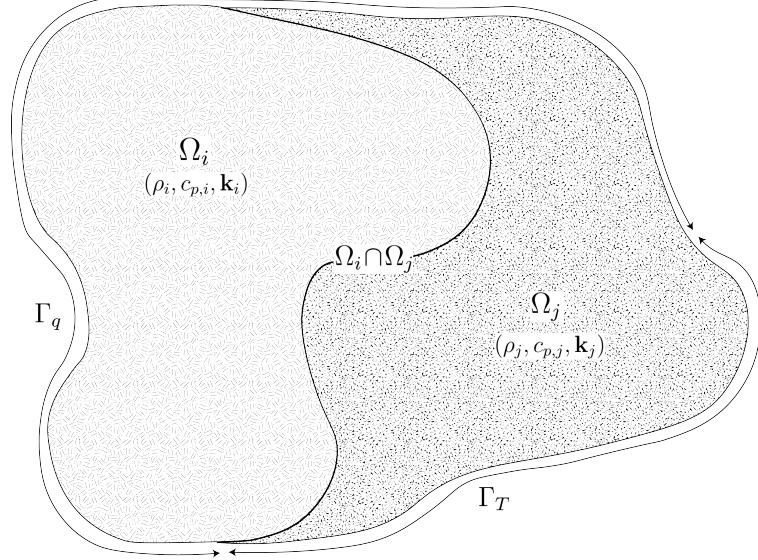


Figure 1: General domain Ω with prescribed Neumann and Dirichlet boundary conditions on Γ_q and Γ_T . Mesh displacement $w(x, t)$ occurs on the Γ_q boundary.

63 2.1 Governing Equations

64 The multi-physics for a non-decomposing ablating TPS involves the transient heat conduction
 65 coupled with mesh motion due to surface recession. The governing equations for the
 66 ablating TPS are summarized in this section.

67 **Heat Conduction** Consider a generic domain $\Omega \subset \mathbb{R}^d$, $d = 2$ or 3 , illustrated in Fig. 1. Let
 68 $\partial\Omega = \Gamma_q \cup \Gamma_T$ and $\Gamma_q \cap \Gamma_T = \emptyset$, where a Neumann $q_b(x, t)$ boundary condition is prescribed on
 69 the Γ_q boundary, and a Dirichlet $T_b(x, t)$ boundary condition is prescribed on the boundary
 70 Γ_T . The ALE establishes that mesh displacements $w(x, t) \in \mathbb{R}^d$ and velocities $v(x, t) \in \mathbb{R}^d$
 71 evolve independently of the physical material's displacements, which are set to zero [CITE](#).

72 The transient heat conduction is described by the energy equation,

$$\rho c_p \left(\frac{\partial T}{\partial t} - v(x, t) \cdot \nabla T \right) - \nabla \cdot (\mathbf{k} \nabla T) = \mathcal{Q}(x, t), \quad x \in \Omega \quad (1a)$$

$$-\mathbf{k} \nabla T \cdot \mathbf{n} = q_b(x, t), \quad x \in \Gamma_q \quad (1b)$$

$$T(x, t) = T_b(x, t), \quad x \in \Gamma_T \quad (1c)$$

$$T(x, 0) = T_0(x), \quad x \in \Omega \quad (1d)$$

73 where the density ρ is constant, while the heat capacity c_p and thermal conductivity $\mathbf{k} \in \mathbb{R}^{d \times d}$,
 74 are temperature dependent. In the order they appear, the terms in eq. (1a) include, the
 75 unsteady energy storage, heat conduction, temperature advection due to mesh motion, and

⁷⁶ source terms due to boundary conditions. The boundary conditions for the energy equation
⁷⁷ includes Neumann eq. (1b) on Γ_1 and Dirichlet eq. (1c) on Γ_T .

⁷⁸ **Mesh Motion** The mesh motion is described by the pseudo-elasticity equation,

$$\nabla \cdot \sigma(w) = 0 \quad (2a)$$

$$w(x, t) = w_q(x, t), \quad x \in \Gamma_q \quad (2b)$$

$$w(x, t) = 0, \quad x \notin \Gamma_q \quad (2c)$$

$$w(x, 0) = \mathbf{0} \quad (2d)$$

⁷⁹ where the stress tensor σ is related to the strain tensor $\epsilon(w)$ through Hooke's law,

$$\sigma(w) = \mathbb{D} : \epsilon(w)$$

⁸⁰ where \mathbb{D} is the constitutive operator, “ $:$ ” is the double contraction of tensors, and ϵ is the
⁸¹ symmetric strain tensor given by,

$$\epsilon(\mathbf{w}) = \frac{1}{2} (\nabla \mathbf{w} + \nabla \mathbf{w}^T)$$

⁸² The “material” properties for the mesh are chosen to tailor the mesh deformation, and need
⁸³ not represent the actual material being modeled Amar2016.

⁸⁴ Ablating effects on the energy equation are handled using the Arbitrary Lagrangian-
⁸⁵ Eulerian (ALE) description.

⁸⁶ The ablation is modeled as mesh motion, and occurs only on the heated boundary Γ_q .

⁸⁷ For the pseudo-elasticity equations, the surface velocity due to the ablating material is a
⁸⁸ function of the surface temperature $T_q(x, t)$ for $x \in \Gamma_q$ on the heated boundary. For the i -th
⁸⁹ material component, the surface velocity is imposed based on the following relation,

$$\hat{\mathbf{n}} \cdot \mathbf{v}(x, t) = f(T_q(x, t)), \quad x \in \Gamma_q \quad (3)$$

⁹⁰ where $\hat{\mathbf{n}}$ is the unit normal vector on the heated boundary Γ_q , and f is a function obtained
⁹¹ from tabulated data for the material, commonly referred to as a B' table. The B' table
⁹² provides the recession velocity as a function of surface temperature, and is pre-computed
⁹³ based on high-fidelity simulations of the ablation process for a one-dimensional slab of the
⁹⁴ material, and is independent of the TPS geometry and boundary conditions. The surface

95 displacements are then computed by integrating the surface velocities over time,

$$\mathbf{w}_q(x, t) = \int_0^t \mathbf{v}(x, \tau) d\tau = \int_0^t f(T_q(x, \tau)) d\tau \quad (4)$$

96 2.2 Full-Order Model: Finite-Element Method

97 To obtain the full-order numerical solution, the governing equation is spatially discretized
 98 using variational principles of Discontinuous Galerkin (DG) to result in a high-dimensional
 99 system of ordinary differential equations (ODEs). Note that the choice of DG approach here
 100 is mainly for theoretical convenience in the coarse-graining formulation, and is exclusively
 101 performed on the energy equation as the quantities of interest correspond to the ablating
 102 surface temperatures. In Sec. [x](#), the high-fidelity ablating TPS solution is performed using
 103 standard FEM for both the energy and elasticitiy equations, and the equivalence between
 104 DG and standard FEM is noted upon their convergence.

105 Consider a conforming mesh partition domain, where each element belongs to one and
 106 only one component. Denote the collection of all M elements as $\{E_i\}_{i=1}^M$. In an element E_i ,
 107 its shared boundaries with another element E_j , Neumann BC, and Dirichlet BC are denoted
 108 as e_{ij} , e_{iq} , and e_{iT} , respectively. Lastly, $|e|$ denotes the length ($n_d = 2$) or area ($n_d = 3$) of a
 109 component boundary e .

110 For the i -th element, use a set of P trial functions, such as polynomials, to represent the
 111 temperature distribution,

$$T^{(i)}(x, t) = \sum_{l=1}^P \phi_l^{(i)}(x) u_l^{(i)} \equiv \boldsymbol{\phi}^{(i)}(x)^T \mathbf{u}^{(i)}(t), \quad i = 1, 2, \dots, M \quad (5)$$

112 By standard variational processes, e.g., [Cohen2018](#), the element-wise governing equation is
 113 denoted as,

$$\mathbf{A}^{(i)} \dot{\mathbf{u}}^{(i)} = (\mathbf{B}^{(i)} + \mathbf{C}^{(i)}) \mathbf{u}^{(i)} + \sum_{j \in \mathcal{N}_i \cup \{T_b\}} \left(\mathbf{B}_{ij}^{(i)} \mathbf{u}^{(i)} + \mathbf{B}_{ij}^{(j)} \mathbf{u}^{(j)} \right) + \mathbf{f}^{(i)}(t), \quad \text{for } i = 1, 2, \dots, M \quad (6)$$

114 which is collected as the following ODE for the all the elements in the mesh,

$$\mathbf{A}(\mathbf{u}) \dot{\mathbf{u}} = [\mathbf{B}(\mathbf{u}) + \mathbf{C}(\mathbf{u})] \mathbf{u} + \mathbf{f}(t) \quad (7)$$

115 where $\mathbf{u} = [\mathbf{u}^{(1)}, \mathbf{u}^{(2)}, \dots, \mathbf{u}^{(M)}]^T \in \mathbb{R}^{MP}$ includes all the DG variables, $\mathbf{f} \in \mathbb{R}^{MP}$ is the
 116 external forcing, and the system matrices \mathbf{A} , \mathbf{B} , and \mathbf{C} are the matrices due to heat capacity,
 117 heat conduction, and temperature advection due to mesh motion, respectively. A detailed

¹¹⁸ derivation of eqs. (6) and (7) and their matrices is provided in Appendix [?].

¹¹⁹ 2.3 Reduced-Physics Model

¹²⁰ The RPM for predicting the response of the ablating TPS consists of two components: (1) the
¹²¹ LCM, and (2) tabulated data for ablating velocity as a function of surface temperature. The
¹²² LCM is described as a first-order system of ODEs for predicting the average temperatures
¹²³ inside the ablating TPS, and provides a low-fidelity under-estimation for the ablating surface
¹²⁴ temperature. The temperature prediction from LCM is used in a B' table to determine the
¹²⁵ surface recession velocity, from which the displacements are obtained through integration.

¹²⁶ 2.3.1 Lumped Capacitance Model

¹²⁷ The main results regarding the LCM are provided in this section; details of the implementa-
¹²⁸ tion for the TPS in Fig. 2 are provided in Appendix A. The LCM is a classical physics-based
¹²⁹ low-order model for predicting the temporal variation of average temperature in multiple in-
¹³⁰ terconnected components INCROPERA. The LCM is derived at the component level from
¹³¹ a point of view of energy conservation, and leads to the following system of ODEs for the
¹³² average temperatures on the components,

$$\bar{\mathbf{A}}\dot{\bar{\mathbf{u}}} = \bar{\mathbf{B}}(\bar{\mathbf{u}})\bar{\mathbf{u}} + \bar{\mathbf{f}}(t) \quad (8)$$

¹³³ where,

$$\bar{\mathbf{u}} = [\bar{u}^{(1)}, \bar{u}^{(2)}, \dots, \bar{u}^{(N)}]^T \in \mathbb{R}^N \quad (9a)$$

$$\bar{\mathbf{f}} = [\bar{f}^{(1)}, \bar{f}^{(2)}, \dots, \bar{f}^{(N)}]^T \in \mathbb{R}^N \quad (9b)$$

¹³⁴ includes the average temperatures $\bar{\mathbf{u}}$ and forcing inputs $\bar{\mathbf{f}}$ for the N components. For $i, j =$
¹³⁵ $1, 2, \dots, N$ the (i, j) -th elements of the $\bar{\mathbf{A}} \in \mathbb{R}^{N \times N}$, $\bar{\mathbf{B}} \in \mathbb{R}^{N \times N}$, and $\bar{\mathbf{f}} \in \mathbb{R}^N$ matrices are
¹³⁶ given by,

$$\bar{A}^{(i)} = \begin{cases} \int_{\Omega^{(i)}} \rho c_p d\Omega^{(i)}, & i = j \\ 0, & i \neq j \end{cases}, \quad \bar{B}_{ij} = \begin{cases} \sum_{j \in \mathcal{N}_i \cup \{T_b\}} \bar{B}_{ij}^{(i)}, & i = j \\ \bar{B}_{ij}^{(j)}, & i \neq j \end{cases}, \quad (10a)$$

$$\bar{\mathbf{f}}^{(i)} = \begin{cases} |e_{iq}| \bar{q}^{(i)} + \frac{|e_{iT}|}{R_i} \bar{T}^{(i)}, & i = j \\ 0, & i \neq j \end{cases} \quad (10b)$$

¹³⁷ where,

$$\bar{q}^{(i)} = \frac{1}{|e_{iq}|} \int_{e_{iq}} q_b de_{iq}, \quad \bar{T}^{(i)} = \frac{1}{|e_{iT}|} \int_{e_{iT}} T_b de_{iT}, \quad \bar{B}_{ij}^{(i)} = -\frac{|e_{ij}|}{R_{ij}}, \quad \bar{B}_{ij}^{(j)} = \frac{|e_{ij}|}{R_{ij}} \quad (11)$$

¹³⁸ 2.3.2 Surface Recession Velocity and Displacements

¹³⁹ The surface velocity on the heated boundary Γ_q is computed based on the temperature
¹⁴⁰ predicted by the LCM using eq. (3). Thus, based on the i -th average temperature $\bar{u}^{(i)}$, the
¹⁴¹ wall-normal surface velocity is computed as,

$$\hat{\mathbf{n}} \cdot \mathbf{v}^{(i)}(x, t) = f(\bar{u}^{(i)}(t)) \quad (12)$$

¹⁴² Due

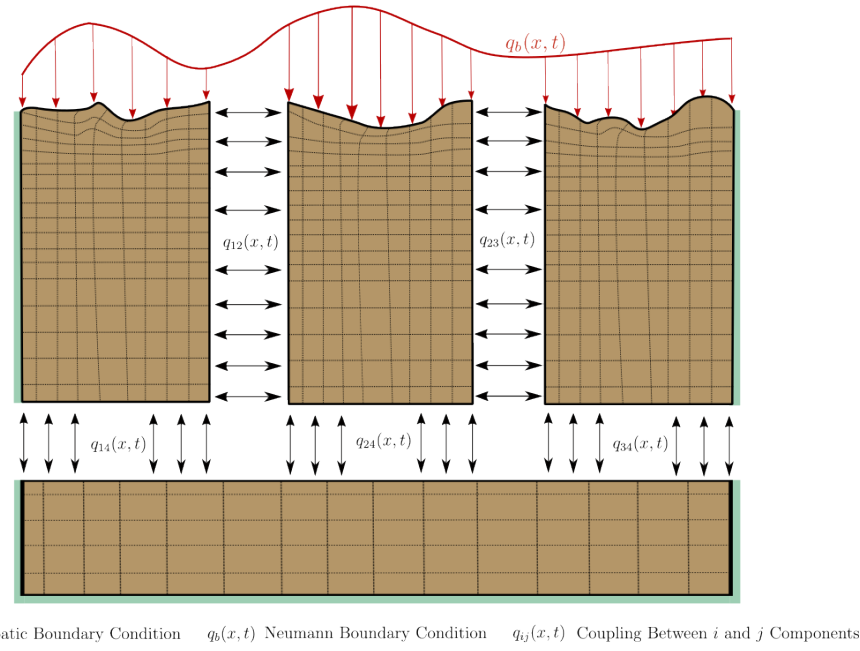
¹⁴³ 2.4 Summary of Modeling Approaches

¹⁴⁴ The FOM (i.e., DG-FEM) and RPM (i.e., LCM) are two different but mathematically con-
¹⁴⁵ nected solution strategies. Specifically, the LCM in eq. (8) not only resembles the functional
¹⁴⁶ form of the DG model in eq. (7), but can be viewed as a special case of the latter, where the
¹⁴⁷ mesh partition is extremely coarse, and the trial and test functions are piece-wise constants.
¹⁴⁸ For example, consider the case where each component $\Omega^{(i)}$ is treated as one single element,
¹⁴⁹ and each element employs one constant basis function $\phi^{(i)} = 1$. The element-wise DG model
¹⁵⁰ in eq. (6) simplifies into a scalar ODE that ignores advection effects due to mesh motion,

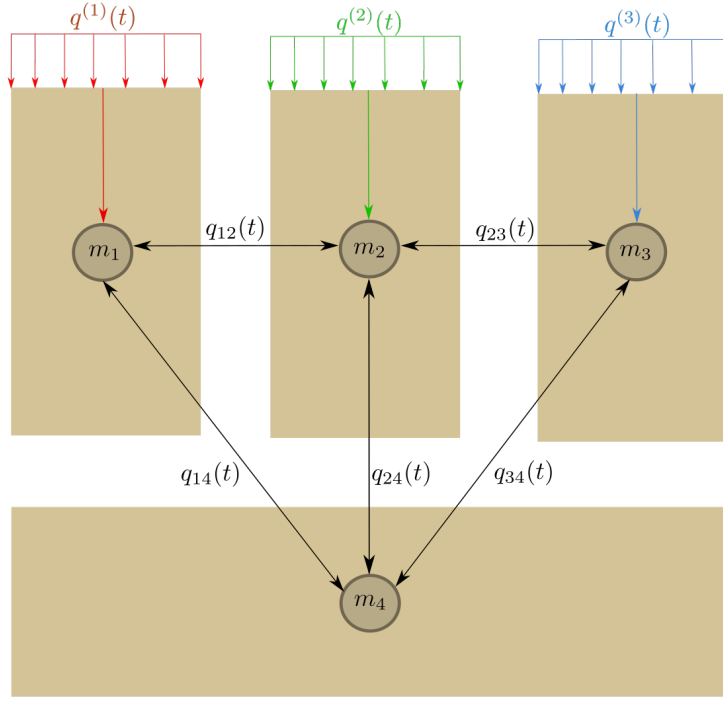
$$\mathbf{A}^{(i)} = \bar{A}^{(i)}, \quad \mathbf{C}^{(i)} = 0, \quad \mathbf{B}_{ij}^{(i)} = -\sigma|e_{ij}|, \quad \mathbf{B}_{ij}^{(j)} = \sigma|e_{ij}|, \quad \mathbf{f}^{(i)} = |e_{iq}|\bar{q}^{(i)} + \sigma|e_{iT}|\bar{T}^{(i)} \quad (13)$$

¹⁵¹ Clearly, the LCM is a coarse zeroth-order DG model with the inverse of thermal resistance
¹⁵² chosen as the element-wise penalty factors. Or conversely, the DG model is a refined version
¹⁵³ of LCM via *hp*-adaptation.

¹⁵⁴ The FOM and RPM represent two extremes in the modeling fidelity and computational
¹⁵⁵ cost spectrum. On one hand, the FOM is the most accurate but computationally expensive
¹⁵⁶ to evaluate due to the fine mesh discretizations for both the temperature and displacement
¹⁵⁷ fields, leading to possibly millions of state variables. On the other hand, the RPM considers
¹⁵⁸ only the average temperature of the material as the state variable, considerably reducing
¹⁵⁹ the computational cost, but sacrificing local temperature information and thus neglecting
¹⁶⁰ higher-order effects due to mesh motion. Thus, neither the FOM nor the RPM is a universal
¹⁶¹ approach for real-world analysis, design, and optimization tasks for ablating TPS, where



(a) TPS Decomposition



(b) Lumped Mass Representation

Figure 2: Partition of the TPS into three ablating and one non-ablating components with the corresponding lumped-mass representation.

162 thousands of high-fidelity model evaluations may be necessary. This issue motivates the
163 development of the PIROM, which can achieve the fidelity of FOM at a computational cost
164 close to the RPM, while maintaining the generalizability to model parameters.

165 3 Physics-Infused Reduced-Order Modeling

166 The formulation of PIROM for ablating TPS starts by connecting the FOM, i.e., DG-FEM,
167 and the RPM, i.e., the LCM, via a coarse-graining procedure. This procedure pinpoints
168 the missing dynamics in the LCM when compared to DG-FEM. Subsequently, the Mori-
169 Zwanzig (MZ) formalism is employed to determine the model form for the missing dynamics
170 in PIROM. Lastly, the data-driven identification of the missing dynamics in PIROM is
171 presented.

172 3.1 Deriving the Reduced-Physics Model via Coarse-Graining

173 The LCM is derived from a full-order DG on a fine mesh via coarse graining. This pro-
174 cess constraints the trial function space of a full-order DG model to a subset of piece-wise
175 constants, so that the variables \mathbf{u} , matrices \mathbf{A} , \mathbf{B} , and \mathbf{C} , and forcing vector \mathbf{f} are all ap-
176 proximated using a single state associated to the average temperature. The details of the
177 projection are described next.

178 3.1.1 Coarse-Graining of States

179 Consider a DG model as in eq. (7) for M elements and an LCM as in eq. (8) for N components;
180 clearly $M \gg N$. Let $\mathcal{V}_j = \{i | E_i \in \Omega_j\}$ be the indices of the elements belonging to the j -th
181 component, so $E_i \in \Omega_j$ for all $i \in \mathcal{V}_j$. The number of elements in the j -th component is $|\mathcal{V}_j|$.
182 The average temperature on Ω_j is,

$$\bar{u}_j = \frac{1}{|\Omega_j|} \sum_{i \in \mathcal{V}_j} \int_{E^{(i)}} \boldsymbol{\phi}^{(i)}(x)^T \mathbf{u}^{(i)} d\Omega = \frac{1}{|\Omega_j|} \sum_{i \in \mathcal{V}_j} |E_i| \boldsymbol{\varphi}_i^{j\top} \mathbf{u}^{(i)}, \quad j = 1, 2, \dots, N \quad (14)$$

183 where $|\Omega_j|$ and $|E_i|$ denote the area ($d = 2$) or volume ($d = 3$) of component j and element
184 i , respectively. The orthogonal basis functions are defined as $\boldsymbol{\varphi}_i^{j\top} = [1, 0, \dots, 0]^\top \in \mathbb{R}^P$.

185 Conversely, given the average temperatures of the N components, $\bar{\mathbf{u}}$, the states of an
186 arbitrary element E_i is written as,

$$\mathbf{u}^{(i)} = \sum_{k=1}^N \boldsymbol{\varphi}_i^k \bar{u}_k + \delta \mathbf{u}^{(i)}, \quad i = 1, 2, \dots, M \quad (15)$$

¹⁸⁷ where $\varphi_i^k = 0$ if $i \notin \mathcal{V}_k$, and $\delta\mathbf{u}^{(i)}$ represents the deviation from the average temperature and
¹⁸⁸ satisfies the orthogonality condition $\varphi_i^{k\top} \delta\mathbf{u}^{(i)} = 0$ for all k .

¹⁸⁹ Equations eqs. (14) and (15) are combined and written in matrix form as,

$$\bar{\mathbf{u}} = \Phi^+ \mathbf{u}, \quad \mathbf{u} = \Phi \mathbf{u} + \delta\mathbf{u} \quad (16)$$

¹⁹⁰ where $\Phi \in \mathbb{R}^{MP \times N}$ is a matrix of $M \times N$ blocks, with the (i, j) -th block as φ_i^j , $\Phi^+ \in \mathbb{R}^{N \times MP}$
¹⁹¹ is the left inverse of Φ , with the (i, j) -th block as $\varphi_i^{j+} = \frac{|E_i|}{|\Omega_j|} \varphi_i^{j\top}$, and $\delta\mathbf{u}$ is the collection of
¹⁹² deviations. By their definitions, $\Phi^+ \Phi = \mathbf{I}$ and $\Phi^+ \delta\mathbf{u} = \mathbf{0}$.

¹⁹³ 3.1.2 Coarse-Graining of Dynamics

¹⁹⁴ Next, consider a function of states in the form of $\mathbf{M}(\mathbf{u})\mathbf{g}(\mathbf{u})$, where $\mathbf{g} : \mathbb{R}^{MP} \rightarrow \mathbb{R}^{MP}$
¹⁹⁵ is a vector-valued function, and $\mathbf{M} : \mathbb{R}^{MP} \rightarrow \mathbb{R}^{p \times MP}$ is a matrix-valued function with an
¹⁹⁶ arbitrary dimension p . Define the projection matrix $\mathbf{P} = \Phi \Phi^+$ and the projection operator
¹⁹⁷ \mathcal{P} as,

$$\begin{aligned} \mathcal{P} [\mathbf{M}(\mathbf{u})\mathbf{g}(\mathbf{u})] &= \mathbf{M}(\mathbf{P}\mathbf{u})\mathbf{g}(\mathbf{P}\mathbf{u}) \\ &= \mathbf{M}(\Phi\bar{\mathbf{u}})\mathbf{g}(\Phi\bar{\mathbf{u}}) \end{aligned} \quad (17)$$

¹⁹⁸ so that the resulting function depends only on the average temperatures $\bar{\mathbf{u}}$. Correspondingly,
¹⁹⁹ the residual operator $\mathcal{Q} = \mathcal{I} - \mathcal{P}$, and $\mathcal{Q}[\mathbf{M}(\mathbf{u})\mathbf{g}(\mathbf{u})] = \mathbf{M}(\mathbf{u})\mathbf{g}(\mathbf{u}) - \mathbf{M}(\Phi\bar{\mathbf{u}})\mathbf{g}(\Phi\bar{\mathbf{u}})$. When
²⁰⁰ the function is not separable, the projection operator is simply defined as $\mathcal{P}[\mathbf{g}(\mathbf{u})] = \mathbf{g}(\mathbf{P}\mathbf{u})$.

²⁰¹ Subsequently, the operators defined above are applied to coarse-grain the dynamics. First,
²⁰² write the DG-FEM in eq. (7) as,

$$\dot{\mathbf{u}} = \mathbf{A}(\mathbf{u})^{-1} \mathbf{B}(\mathbf{u}) \mathbf{u} + \mathbf{A}(\mathbf{u})^{-1} \mathbf{C}(\mathbf{u}) \mathbf{u} + \mathbf{A}(\mathbf{u})^{-1} \mathbf{f}(t) \quad (18)$$

²⁰³ and multiply both sides by Φ^+ to obtain,

$$\Phi^+ \dot{\mathbf{u}} = \Phi^+ (\Phi \dot{\bar{\mathbf{u}}} + \delta \dot{\mathbf{u}}) = \dot{\bar{\mathbf{u}}} = \Phi^+ \mathbf{r}(\mathbf{u}, t) \quad (19)$$

²⁰⁴ Apply the projection operator \mathcal{P} and the residual operator \mathcal{Q} to the right-hand side to obtain,

$$\dot{\bar{\mathbf{u}}} = \mathcal{P} [\Phi^+ \mathbf{r}(\mathbf{u}, t)] + \mathcal{Q} [\Phi^+ \mathbf{r}(\mathbf{u}, t)] \equiv \mathbf{r}^{(1)}(\mathbf{u}, t) + \mathbf{r}^{(2)}(\mathbf{u}, t) \quad (20)$$

²⁰⁵ where $\mathbf{r}^{(1)}(\mathbf{u}, t)$ is resolved dynamics that depends on $\bar{\mathbf{u}}$ only, and $\mathbf{r}^{(2)}(\mathbf{u}, t)$ is the un-resolved
²⁰⁶ or residual dynamics. Detailed derivations and analysis of $\mathbf{r}^{(1)}(\mathbf{u}, t)$ and $\mathbf{r}^{(2)}(\mathbf{u}, t)$ can be

207 found in the Appendix.

208 It follows from Ref. x that the resolved dynamics is exactly the LCM, where the advection
 209 term reduces to zero, i.e., $\bar{\mathbf{C}}(\bar{\mathbf{u}}) = \mathbf{0}$ as shown in the Appendix. Using the notation from
 210 eq. (8), it follows that,

$$\begin{aligned}\mathbf{r}^{(1)}(\mathbf{u}, t) &= \bar{\mathbf{A}}(\bar{\mathbf{u}})^{-1}\bar{\mathbf{B}}(\bar{\mathbf{u}})\bar{\mathbf{u}} + \bar{\mathbf{A}}(\bar{\mathbf{u}})^{-1}\bar{\mathbf{C}}(\bar{\mathbf{u}})\bar{\mathbf{u}} + \bar{\mathbf{A}}(\bar{\mathbf{u}})^{-1}\bar{\mathbf{f}}(\bar{\mathbf{u}}) \\ &= \bar{\mathbf{A}}(\bar{\mathbf{u}})^{-1}\bar{\mathbf{B}}(\bar{\mathbf{u}})\bar{\mathbf{u}} + \bar{\mathbf{A}}(\bar{\mathbf{u}})^{-1}\bar{\mathbf{f}}(t)\end{aligned}\quad (21)$$

211 where the following relations hold,

$$\bar{\mathbf{A}}(\bar{\mathbf{u}}) = \mathbf{W} (\Phi^+ \mathbf{A} (\Phi \bar{\mathbf{u}})^{-1} \Phi)^{-1} \quad \bar{\mathbf{C}}(\bar{\mathbf{u}}) = \mathbf{0} \quad (22a)$$

$$\bar{\mathbf{B}}(\bar{\mathbf{u}}) = \mathbf{W} \Phi^+ \mathbf{B} (\Phi \bar{\mathbf{u}}) \Phi \quad \bar{\mathbf{f}}(t) = \mathbf{W} \Phi^+ \mathbf{f} \quad (22b)$$

212 where $\mathbf{W} \in \mathbb{R}^{N \times N}$ is a diagonal matrix with the i -th element as $[\mathbf{W}]_{ii} = |\mathcal{V}_k|$ if $i \in$
 213 \mathcal{V}_k . As shown in the Appendix, the examination of the second residual term $\mathbf{r}^{(2)}(\mathbf{u}, t)$ in
 214 eq. (20) reveals the physical sources of missing dynamics in the LCM: the approximation of
 215 non-uniform temperature within each component as a constant, and the elimination of the
 216 advection term due to coarse-graining.

217 In sum, the above results not only show that the LCM is a result of coarse-graining of
 218 the full-order DG-FEM, but also reveal the discrepancies between the LCM and the DG-
 219 FEM. In the subsequent section, the discrepancies will be corrected to produce the proposed
 220 PIROM.

221 3.2 Formulation of Reduced-Order Model

222 The Mori-Zwanzig (MZ) formalism is an operator-projection technique used to derive ROMs
 223 for high-dimensional dynamical systems, especially in statistical mechanics and fluid dynam-
 224 ics Parish,Duraisamy . It provides an exact reformulation of the full-order dynamics in terms
 225 of a subset of resolved variables. The proposed ROM is subsequently developed based on
 226 such reformulation. Equation eq. (20) shows that the DG-FEM dynamics can be decomposed
 227 into the resolved dynamics $\mathbf{r}^{(1)}(\mathbf{u}, t)$ and the orthogonal dynamics $\mathbf{r}^{(2)}(\mathbf{u}, t)$, in the sense of
 228 $\mathcal{P}\mathbf{r}^{(2)} = 0$. In this case, the MZ formalism can be invoked to express the dynamics $\bar{\mathbf{u}}$ in terms
 229 of $\bar{\mathbf{u}}$ alone as the projected Generalized Langevin Equation (GLE) Parish,Duraisamy ,

$$\dot{\bar{\mathbf{u}}}(t) = \mathbf{r}^{(1)}(\bar{\mathbf{u}}, t) + \int_0^t \tilde{\kappa}(t, s, \bar{\mathbf{u}}) ds \quad (23)$$

230 where the first term is Markovian, and the integral term is referred to as the memory. The
 231 integral term is non-Markovian, accounting for impact of past resolved states on the current
 232 states through their interactions with the un-resolved states.

233 Next, to further inform the subsequent derivation of the ROM, the kernel $\tilde{\mathbf{k}}$ is examined
 234 via a leading-order expansion, based on prior work $\textcolor{blue}{x}$; this can be viewed as an analog of
 235 zeroth-order holding in linear system theory with a sufficiently small time step. In this case,
 236 the memory kernel is approximated as,

$$\tilde{\kappa}(t, s, \bar{\mathbf{u}}) \approx \mathbf{r}^{(1)}(\bar{\mathbf{u}}, t) \cdot \nabla_{\bar{\mathbf{u}}} \mathbf{r}^{(2)}(\Phi \bar{\mathbf{u}}, t) \quad (24)$$

237 Note that the terms in $\mathbf{r}^{(1)}$ have a common factor $\bar{\mathbf{A}}^{-1}$; this motivates the following heuristic
 238 modification of the model form in eq. (23),

$$\dot{\bar{\mathbf{u}}} = \mathbf{r}^{(1)}(\bar{\mathbf{u}}, t) + \bar{\mathbf{A}}^{-1}(\bar{\mathbf{u}}) \int_0^t \kappa(t, s, \bar{\mathbf{u}}) ds \quad (25a)$$

$$\bar{\mathbf{A}}(\bar{\mathbf{u}}) \dot{\bar{\mathbf{u}}} = \bar{\mathbf{B}}(\bar{\mathbf{u}}) \bar{\mathbf{u}} + \bar{\mathbf{f}}(t) + \int_0^t \kappa(t, s, \bar{\mathbf{u}}) ds \quad (25b)$$

239 where the original kernel $\tilde{\kappa}$ is effectively normalized by $\bar{\mathbf{A}}^{-1}$. Intuitively, such choice of kernel
 240 reduces its dependency on the averaged material properties, and simplifies the subsequent
 241 design of model form.

242 Subsequently, the hidden states are introduced to “Markovianize” the system eq. (23).
 243 In this manner, eq. (25b) is converted into a pure state-space model, with the functional
 244 form of the LCM retained; since LCM is a physics-based model, then it encodes the phys-
 245 ical information and retains explicit parametric dependence of the problem. Consider the
 246 representation of the kernel as a finite sum of simpler functions, e.g., exponentials,

$$\kappa(t, s, \bar{\mathbf{u}}) = \sum_{j=1}^m \mathcal{K}_j(t, s, \bar{\mathbf{u}}) [\mathbf{p}_j + \mathbf{d}_j(\bar{\mathbf{u}})] \phi_j(s, \bar{\mathbf{u}}) \quad (26)$$

247 where,

$$\mathcal{K}_j(t, s, \bar{\mathbf{u}}) = e^{-\int_s^t (\lambda_j + e_j(\bar{\mathbf{u}})) d\tau}, \quad \phi_j(s, \bar{\mathbf{u}}) = \mathbf{q}_j^\top \bar{\mathbf{u}}(s) + \mathbf{g}_j(\bar{\mathbf{u}})^\top \bar{\mathbf{u}}(s) + \mathbf{r}_j^\top \bar{\mathbf{f}}(s) \quad (27)$$

248 with suitable coefficients $\mathbf{p}_j, \mathbf{d}_j, \mathbf{q}_j, \mathbf{g}_j, \mathbf{r}_j \in \mathbb{R}^N$ and decay rates $\lambda_j, e_j(\bar{\mathbf{u}}) > 0$, that need to
 249 be identified from data.

250 Define the hidden states as,

$$\beta_j(t) = \int_0^t \mathcal{K}_j(s, \bar{\mathbf{u}}) \phi_j(s, \bar{\mathbf{u}}) ds \quad (28)$$

251 then through its differentiation with respect to time,

$$\dot{\beta}_j(t) = -[\lambda_j + e_j(\bar{\mathbf{u}})] \beta_j(t) + \mathbf{q}_j^\top \bar{\mathbf{u}}(t) + \mathbf{g}_j(\bar{\mathbf{u}})^\top \bar{\mathbf{u}}(t) + \mathbf{r}_j^\top \bar{\mathbf{f}}(t) \quad (29)$$

252 and the memory term becomes,

$$\int_0^t \boldsymbol{\kappa}(t, s, \bar{\mathbf{u}}) ds = \sum_{j=1}^m [\mathbf{p}_j + \mathbf{d}_j(\bar{\mathbf{u}})] \beta_j(t) \quad (30)$$

253 Then, eq. (25b) is recast as the extended Markovian system,

$$\bar{\mathbf{A}}(\bar{\mathbf{u}}) \dot{\bar{\mathbf{u}}} = \bar{\mathbf{B}}(\bar{\mathbf{u}}) \bar{\mathbf{u}} + [\mathbf{P} + \mathbf{D}(\bar{\mathbf{u}})] \boldsymbol{\beta} + \bar{\mathbf{f}}(t) \quad (31a)$$

$$\dot{\boldsymbol{\beta}} = [-\boldsymbol{\Lambda} + \mathbf{E}(\bar{\mathbf{u}})] \boldsymbol{\beta} + [\mathbf{Q} + \mathbf{G}(\bar{\mathbf{u}})] \bar{\mathbf{u}} + \mathbf{R} \bar{\mathbf{f}}(t) \quad (31b)$$

254 where,

$$\boldsymbol{\Lambda} = \text{diag}(\lambda_1, \lambda_2, \dots, \lambda_m) \in \mathbb{R}^{m \times m}, \quad \mathbf{P} = [\mathbf{p}_1, \mathbf{p}_2, \dots, \mathbf{p}_m] \in \mathbb{R}^{N \times m} \quad (32a)$$

$$\mathbf{D}(\bar{\mathbf{u}}) = [\mathbf{d}_1(\bar{\mathbf{u}}), \mathbf{d}_2(\bar{\mathbf{u}}), \dots, \mathbf{d}_m(\bar{\mathbf{u}})] \in \mathbb{R}^{N \times m}, \quad \mathbf{Q} = [\mathbf{q}_1, \mathbf{q}_2, \dots, \mathbf{q}_m] \in \mathbb{R}^{m \times N} \quad (32b)$$

$$\mathbf{G}(\bar{\mathbf{u}}) = [\mathbf{g}_1(\bar{\mathbf{u}}), \mathbf{g}_2(\bar{\mathbf{u}}), \dots, \mathbf{g}_m(\bar{\mathbf{u}})] \in \mathbb{R}^{m \times N}, \quad \mathbf{R} = [\mathbf{r}_1, \mathbf{r}_2, \dots, \mathbf{r}_m] \in \mathbb{R}^{m \times N} \quad (32c)$$

$$\mathbf{E}(\bar{\mathbf{u}}) = \text{diag}(e_1(\bar{\mathbf{u}}), e_2(\bar{\mathbf{u}}), \dots, e_m(\bar{\mathbf{u}})) \in \mathbb{R}^{m \times m} \quad (32d)$$

255 Since the hidden states $\boldsymbol{\beta}$ serve as the memory, their initial conditions are set to zero, i.e.,
256 $\boldsymbol{\beta}(t_0) = \mathbf{0}$, no memory at the beginning. The physics-infused model in eq. (31) retains the
257 structure of the LCM, while the hidden states account for missing physics through corrections
258 to the stiffness and advection matrices, as well as the forcing term.

259 Lastly, denote the collection of resolved and hidden states as $\mathbf{y} = [\bar{\mathbf{u}}, \boldsymbol{\beta}]^T \in \mathbb{R}^{n_y}$ with
260 $n_y = N + m$, then the proposed PIROM is summarized as,

$$\tilde{\mathbf{A}} \dot{\mathbf{y}} = [\tilde{\mathbf{B}} + \tilde{\mathbf{C}}] \mathbf{y} + \mathbf{H} \bar{\mathbf{f}}(t) \quad (33a)$$

$$\mathbf{z} = \mathbf{M} \mathbf{y} \quad (33b)$$

261 where,

$$\tilde{\mathbf{A}} = \begin{bmatrix} \bar{\mathbf{A}}(\bar{\mathbf{u}}) & \mathbf{O} \\ \mathbf{O} & \mathbf{I} \end{bmatrix} \in \mathbb{R}^{n_y \times n_y}, \quad \tilde{\mathbf{B}} = \begin{bmatrix} \bar{\mathbf{B}}(\bar{\mathbf{u}}) & \mathbf{P} \\ \mathbf{Q} & -\Lambda \end{bmatrix} \in \mathbb{R}^{n_y \times n_y}, \quad \tilde{\mathbf{C}} = \begin{bmatrix} \mathbf{0} & \mathbf{D}(\bar{\mathbf{u}}) \\ \mathbf{G}(\bar{\mathbf{u}}) & \mathbf{E}(\bar{\mathbf{u}}) \end{bmatrix} \in \mathbb{R}^{n_y \times n_y}, \quad (34a)$$

$$\mathbf{H} = \begin{bmatrix} \mathbf{I} \\ \mathbf{R} \end{bmatrix} \in \mathbb{R}^{n_y \times N}, \quad \mathbf{M} \in \mathbb{R}^{n_z \times n_y} \quad (34b)$$

262 In eq. (33), the terms $\bar{\mathbf{A}}$, $\bar{\mathbf{B}}$, and $\bar{\mathbf{f}}$ are the LCM terms. The collection of matrices,

$$\Theta = \{\mathbf{P}, \mathbf{D}(\bar{\mathbf{u}}), \mathbf{G}(\bar{\mathbf{u}}), \Lambda, \mathbf{E}(\bar{\mathbf{u}}), \mathbf{Q}, \mathbf{G}(\bar{\mathbf{u}}), \mathbf{R}, \mathbf{M}\}, \in \mathbb{R}^{n_\theta} \quad (35)$$

263 are learnable parameters to capture the memory effects. Particularly, the matrices $\mathbf{P}, \Lambda, \mathbf{Q}, \mathbf{R}$
264 are constants that need to be identified from data, and account for the effects of coarse-
265 graining on the stiffness and forcing matrices. The matrices $\mathbf{D}(\bar{\mathbf{u}}), \mathbf{E}(\bar{\mathbf{u}}), \mathbf{G}(\bar{\mathbf{u}})$ are state-
266 dependent matrices, and account for the effects of coarse-graining on the advection matrix.
267 Leveraging the DG-FEM formula for the advection matrix in eq. (44c) in the Appendix, and
268 noting that the mesh displacements are functions of the ablating velocity as in eq. (3), the
269 state-dependent matrices for the i -th component are written as,

$$\mathbf{D}^{(i)}(\bar{\mathbf{u}}) \approx f^{(i)}(\bar{u}^{(i)}) \mathbf{D}^{(i)}, \quad \mathbf{E}^{(i)}(\bar{\mathbf{u}}) \approx f^{(i)}(\bar{u}^{(i)}) \mathbf{E}^{(i)}, \quad \mathbf{G}^{(i)}(\bar{\mathbf{u}}) \approx f^{(i)}(\bar{u}^{(i)}) \mathbf{G}^{(i)} \quad (36)$$

270 where $f^{(i)}(\bar{u}^{(i)})$ is the surface recession velocity function in eq. (12) for the i -th component,
271 and $\mathbf{D}^{(i)}, \mathbf{E}^{(i)}, \mathbf{G}^{(i)}$ are constant matrices to be identified from data. In eq. (33), \mathbf{M} is a
272 fully-populated matrix that extracts the observables, i.e., the surface temperatures, from
273 the PIROM states \mathbf{y} . The PIROM incorporates explicit information on the temperature-
274 dependent material properties through the LCM matrices, as well as the surface recession
275 velocity function through eq. (36). The next step is focused on identifying the unknown
276 parameters Θ characterizing the hidden dynamics.

277 3.3 Learning the Hidden Dynamics from Data

278 The learning of the PIROM is achieved through a neural-ODE like approach [Chen2018](#).
279 For ease of presentation, consider the following compact form of the PIROM in eq. (33),

$$\mathcal{F}(\dot{\mathbf{y}}, \mathbf{y}; \boldsymbol{\xi}, \Theta) = \mathbf{0} \quad (37)$$

280 where $\boldsymbol{\xi}$ defines the parametrization of the problem, i.e., operating conditions, such as the
 281 BC's, as well as the material properties. Consider a dataset of N_s high-fidelity trajectories
 282 of observables over a time interval $[t_0, t_f]$,

$$\mathcal{D} = \left\{ \left(t_k, \mathbf{z}_{\text{HF}}^{(l)}(t_k), \boldsymbol{\xi}^{(l)} \right) \right\}_{l=1}^{N_s}, \quad k = 0, 1, \dots, K \quad (38)$$

283 The learning problem is formulated as the following differentially-constrained problem,

$$\min_{\Theta} \quad \frac{1}{N_s} \sum_{l=1}^{N_s} \frac{1}{K} \sum_{k=0}^K \left\| \mathbf{z}_{\text{HF}}^{(l)}(t_k) - \mathbf{M}\mathbf{y}^{(l)}(t_k) \right\|_2^2 \quad (39a)$$

$$\text{s.t.} \quad \mathcal{F} \left(\dot{\mathbf{y}}^{(l)}, \mathbf{y}^{(l)}; \boldsymbol{\xi}^{(l)}, \Theta \right) = \mathbf{0}, \quad t \in [t_0, t_f], \quad l = 1, 2, \dots, N_s \quad (39b)$$

$$\mathbf{y}^{(l)}(t_0) = \mathbf{y}_0(\boldsymbol{\xi}^{(l)}), \quad l = 1, 2, \dots, N_s \quad (39c)$$

284 **A Technical Details**

285 This appendix presents the technical details of the PIROM framework applied to the TPS
286 ablation problem. The first section provides the mathematical details for the definition of
287 the DG-FEM. The second section follows the projection procedures from Ref. x, and demon-
288 strates the effects of coarse-graining on the advection matrix. The third section presents the
289 derivation of the LCM model from an energy-conservation perspective.

290 **A.1 Full-Order Model**

291 To obtain the full-order numerical solution, the governing equation is spatially discretized
292 using variational principles of Discontinuous Galerkin (DG) to result in a high-dimensional
293 system of ordinary differential equations (ODEs). The DG-FEM model is written in an
294 element-wise form, which is beneficial for subsequent derivations of the lower-order models.
295 Note that the choice of DG approach here is mainly for theoretical convenience in the sub-
296 sequent coarse-graining formulation. In the numerical results, the full-order TPS ablation
297 simulations is computed using standard FEM instead, and the equivalence between DG and
298 standard FEM is noted upon their convergence.

299 **A.1.1 Domain Discretization**

300 Consider a conforming mesh partition of the domain, as shown in Fig. DOMAIN, where each
301 element belongs to one and only one component. Denote the collection of all M elements
302 as $\{E_i\}_{i=1}^M$. To ease the description of the DG model, a graph structure is employed. The
303 elements are treated as vertices, the set of which is denoted $\mathcal{V} = \{m\}_{m=1}^M$. Two neighboring
304 elements, E_i and E_j , are connected by an edge (i, j) , and the shared boundary between them
305 is denoted e_{ij} . The collection of all edges are denoted \mathcal{E} , and \mathcal{G} is referred to as a graph.
306 In the graph, the edges are unidirected, meaning if $(i, j) \in \mathcal{E}$ then $(j, i) \in \mathcal{E}$. Furthermore,
307 denote the neighbors of the i -th element as $\mathcal{N}_i = \{j | (i, j) \in \mathcal{E}\}$. Lastly, for the ease of
308 notation, introduce two special indices: T for the boundary of an element that overlaps with
309 the Dirichlet boundary condition, and similarly q for the Neumann boundary condition.

³¹⁰ **A.1.2 Weak Form of Discontinuous Galerkin Method**

³¹¹ Choosing appropriate basis functions ϕ_k and ϕ_l and using the Interior Penalty Galerkin
³¹² (IPG) scheme [?], the variational bilinear form for eq. (1a) is,

$$\sum_{i=1}^M a_{\epsilon,i}(\phi_k, \phi_l) = \sum_{i=1}^M L_i(\phi_k) \quad (40)$$

³¹³ where ϵ is an user-specified parameter and,

$$a_{\epsilon,i}(\phi_k, \phi_l) = \int_{E^{(i)}} \left(\rho c_p \phi_k \frac{\partial \phi_l}{\partial t} + \nabla \phi_k \cdot (\mathbf{k} \nabla \phi_l) - \rho c_p \phi_k \mathbf{v} \cdot \nabla \phi_l \right) dE^{(i)} \quad (41a)$$

$$\begin{aligned} &= - \sum_{j \in \mathcal{N}_i \cup \{T_b\}} \int_{e_{ij}} \{ \mathbf{k} \nabla \phi_k \cdot n \} [\phi_l] de_{ij} + \epsilon \sum_{j \in \mathcal{N}_i \cup \{T_b\}} \int_{e_{ij}} \{ \mathbf{k} \nabla \phi_l \cdot n \} [\phi_k] de_{ij} \\ &\quad + \sigma \sum_{j \in \mathcal{N}_i \cup \{T_b\}} \int_{e_{ij}} [\phi_k] [\phi_l] de_{ij} \end{aligned} \quad (41b)$$

$$L_i(v) = \epsilon \sum_{j \in \mathcal{N}_i \cup \{T_b\}} \int_{e_{ij}} (\mathbf{k} \nabla \phi_l \cdot n) T_b de_{ij} + \int_{e_{iq}} \phi_k q_b de_{iq} + \sigma \int_{e_{iT}} \phi_k T_b de_{iT} \quad (41c)$$

³¹⁴ In the bi-linear form above, the notations $[]$ and $\{\}$ are respectively the jumps and averages
³¹⁵ at the boundary e_{ij} share by two elements E_i and E_j ,

$$[u] = u|_{E_i} - u|_{E_j}, \quad \{u\} = \frac{1}{2} \left(u|_{E_i} + u|_{E_j} \right), \quad \text{for } x \in e_{ij} = E_i \cap E_j$$

³¹⁶ Furthermore, in the bi-linear form, the terms associated with σ are introduced to enforce
³¹⁷ the Dirichlet boundary conditions; σ is a penalty factor whose value can depend on the size
³¹⁸ of an element. Depending on the choice of ϵ , the bi-linear form corresponds to symmetric
³¹⁹ IPG ($\epsilon = -1$), non-symmetric IPG ($\epsilon = 1$), and incomplete IPG ($\epsilon = 0$). All these schemes
³²⁰ are consistent with the original PDE and have similar convergence rate with respect to mesh
³²¹ size. In the following derivations, the case $\epsilon = 0$ is chosen for the sake of simplicity.

³²² **A.1.3 Discontinuous Galerkin Model**

³²³ Next, the DG-based model is written in an element-wise form. For the i -th element, use a
³²⁴ set of P trial functions to represent the temperature as in eq. (5). Without loss of generality,
³²⁵ the trial functions are assumed to be orthogonal, so that $\int_{E^{(i)}} \phi_k^{(i)}(x) \phi_l^{(i)}(x) dx = |E^{(i)}| \delta_{kl}$,
³²⁶ where $|E^{(i)}|$ is the area ($n_d = 2$) or volume ($n_d = 3$) of the i -th element, and δ_{kl} is the
³²⁷ Kronecker delta.

³²⁸ Using test functions same as trial functions, the dynamics $\mathbf{u}^{(i)}$ is obtained by evaluating

³²⁹ the element-wise bi-linear forms,

$$a_{\epsilon,i}(\phi_k^{(i)}, T^{(i)}) = L_i(\phi_k^{(i)}), \quad k = 1, 2, \dots, P \quad (42)$$

³³⁰ The above procedure yields,

$$\mathbf{A}^{(i)} \dot{\mathbf{u}}^{(i)} = (\mathbf{B}^{(i)} + \mathbf{C}^{(i)}(t)) \mathbf{u}^{(i)} + \sum_{j \in \mathcal{N}_i \cup \{T_b\}} \left(\mathbf{B}_{ij}^{(i)} \mathbf{u}^{(i)} + \mathbf{B}_{ij}^{(j)} \mathbf{u}^{(j)} \right) + \mathbf{f}^{(i)}(t) \quad (43)$$

³³¹ where for $k, l = 1, 2, \dots, P$,

$$[\mathbf{A}^{(i)}]_{kl} = \int_{E^{(i)}} \rho c_p \phi_k^{(i)} \phi_l^{(i)} dE^{(i)} \quad (44a)$$

$$[\mathbf{B}^{(i)}]_{kl} = - \int_{E^{(i)}} (\nabla \phi_k^{(i)}) \cdot (\mathbf{k} \nabla \phi_l^{(i)}) dE^{(i)} \quad (44b)$$

$$[\mathbf{C}^{(i)}]_{kl} = \int_{E^{(i)}} \rho c_p \phi_k^{(i)} \mathbf{v}^{(i)} \cdot \nabla \phi_l^{(i)} dE^{(i)} \quad (44c)$$

$$[\mathbf{B}_{ij}^{(i)}] = \int_{e_{ij}} \left\{ \mathbf{k} \nabla \phi_k^{(i)} \cdot \hat{n} \right\} \phi_l^{(i)} - \sigma [\phi_k^{(i)}] \phi_l^{(i)} de_{ij} \quad (44d)$$

$$[\mathbf{B}_{ij}^{(j)}] = \int_{e_{ij}} - \left\{ \mathbf{k} \nabla \phi_k^{(i)} \cdot \hat{n} \right\} \phi_l^{(j)} + \sigma [\phi_k^{(i)}] \phi_l^{(j)} de_{ij} \quad (44e)$$

$$[\mathbf{f}^{(i)}]_k = \int_{e_{iq}} \phi_k^{(i)} q_b de_{iq} + \sigma \int_{e_{iT}} \phi_k^{(i)} de_{iT} \quad (44f)$$

³³² The matrices $\mathbf{A}^{(i)} \in \mathbb{R}^{P \times P}$, $\mathbf{B}^{(i)} \in \mathbb{R}^{P \times P}$, and $\mathbf{C}^{(i)} \in \mathbb{R}^{P \times P}$ are respectively the capacitance,
³³³ conductivity, and advection matrices for element i . These matrices depend on ρ , c_p , \mathbf{k} , and
³³⁴ \mathbf{v} , and hence can be non-linear functions of $\mathbf{u}^{(i)}$. Since the trial functions are orthogonal, if
³³⁵ ρc_p is constant within an element, $\mathbf{A}^{(i)}$ is diagonal; otherwise, \mathbf{A}_i is symmetric and positive
³³⁶ definite as $\rho c_p > 0$.

³³⁷ For compactness, the element-wise model in eq. (43) is also written in matrix form,

$$\mathbf{A}(\dot{\mathbf{u}}) = [\mathbf{B}(\mathbf{u}) + \mathbf{C}(\mathbf{u})] \mathbf{u} + \mathbf{f}(t) \quad (45)$$

³³⁸ where $\mathbf{u} = [\mathbf{u}^{(1)}, \mathbf{u}^{(2)}, \dots, \mathbf{u}^{(M)}]^T \in \mathbb{R}^{MP}$ includes all DG variables, $\mathbf{f} = [\mathbf{f}^{(1)}, \mathbf{f}^{(2)}, \dots, \mathbf{f}^{(M)}]^T \in \mathbb{R}^{MP}$, \mathbf{A} and \mathbf{C} are matrices of M diagonal blocks whose i -th blocks are $\mathbf{A}^{(i)}$ and $\mathbf{C}^{(i)}$, and
³³⁹ \mathbf{B} is a matrix of $M \times M$ blocks whose (i, j) -th block is,
³⁴⁰

$$\mathbf{B}_{ij} = \begin{cases} \mathbf{B}^{(i)} + \sum_{j \in \mathcal{N}_i \cup \{T_b\}} \mathbf{B}_{ij}^{(i)}, & i = j \\ \mathbf{B}_{ij}^{(j)}, & i \neq j \end{cases} \quad (46)$$

³⁴¹ The dependency of \mathbf{A} , \mathbf{B} , and \mathbf{C} on \mathbf{u} is explicitly noted in eq. (45), which is the source of
³⁴² non-linearity in the current TPS problem. Moreover, the mesh velocity \mathbf{v} varies with space
³⁴³ and time, and thus the advection matrix \mathbf{C} varies with time as a function of q_b .

³⁴⁴ A.2 Coarse-Graining of Dynamics

³⁴⁵ The LCM is obtained by coarse-graining the full-order DG-FEM. This coarse-graining proce-
³⁴⁶ dure produces resolved $\mathbf{r}^{(1)}(\mathbf{u}, t)$ and residual $\mathbf{r}^{(2)}(\mathbf{u}, t)$ dynamics as in eq. (20). This section
³⁴⁷ presents the detail derivations and magnitude analysis for the resolved and residual dynam-
³⁴⁸ ics.

³⁴⁹ A.2.1 Resolved Dynamics

³⁵⁰ Using eq. (17), the resolved dynamics is computed as follows,

$$\mathbf{r}^{(1)}(\mathbf{u}, t) = \mathcal{P} [\Phi^+ \mathbf{A}(\mathbf{u})^{-1} (\mathbf{B}(\mathbf{u})\mathbf{u} + \mathbf{C}(\mathbf{u})\mathbf{u} + \mathbf{f}(t))] \quad (47a)$$

$$\begin{aligned} &= \Phi^+ \mathbf{A}(\mathbf{Pu})^{-1} \mathbf{PB}(\mathbf{Pu}) \mathbf{Pu} + \Phi^+ \mathbf{A}(\mathbf{Pu})^{-1} \mathbf{PC}(\mathbf{Pu}) \mathbf{Pu} \\ &\quad + \Phi^+ \mathbf{A}(\mathbf{Pu})^{-1} \mathbf{Pf}(t, \mathbf{Pu}) \end{aligned} \quad (47b)$$

$$\begin{aligned} &= \underbrace{\Phi^+ \mathbf{A}(\Phi \bar{\mathbf{u}})^{-1} \Phi}_{\#1} \underbrace{\Phi^+ \mathbf{B}(\Phi \bar{\mathbf{u}}) \Phi \bar{\mathbf{u}}}_{\#2} + \Phi^+ \mathbf{A}(\Phi \bar{\mathbf{u}})^{-1} \Phi \underbrace{\Phi^+ \mathbf{C}(\Phi \bar{\mathbf{u}}) \Phi \bar{\mathbf{u}}}_{\#3} \\ &\quad + \Phi^+ \mathbf{A}(\Phi \bar{\mathbf{u}})^{-1} \Phi \underbrace{\Phi^+ \mathbf{f}(t, \Phi \bar{\mathbf{u}})}_{\#4} \end{aligned} \quad (47c)$$

³⁵¹ Detailed derivations for the #1, #2, and #4 terms can be found in Ref. [x](#). The effects of
³⁵² coarse-graining on the advection term #3 are analyzed next.

³⁵³ **Term #3** The $\mathbf{C}(\mathbf{u}) \in \mathbb{R}^{MP \times MP}$ matrix contains M diagonal of size $P \times P$, since the
³⁵⁴ basis functions are defined locally on each element. Therefore, $[\mathbf{C}(\mathbf{u})]_{ij} = \mathbf{0}$ for all $i \neq j$ with
³⁵⁵ $i, j = 1, 2, \dots, M$. It follows that for $k, l = 1, 2, \dots, N$,

$$[\Phi^+ \mathbf{C}(t, \Phi \bar{\mathbf{u}}) \Phi]_{kl} = \sum_{i=1}^M \sum_{j=1}^M \boldsymbol{\varphi}_i^{k+} [\mathbf{C}(t, \Phi \bar{\mathbf{u}})]_{ij} \boldsymbol{\varphi}_j^l \quad (48a)$$

$$= \sum_{i=1}^M \boldsymbol{\varphi}_i^{k+} [\mathbf{C}(t, \Phi \bar{\mathbf{u}})]_{ii} \boldsymbol{\varphi}_i^l \quad (48b)$$

$$= \sum_{i \in \mathcal{V}_k} \boldsymbol{\varphi}_i^{k+} [\mathbf{C}(t, \Phi \bar{\mathbf{u}})]_{ii} \boldsymbol{\varphi}_i^l \quad (48c)$$

where in the second row, the fact that $[\mathbf{C}(\mathbf{u})]_{ij} = 0$ for all $i \neq j$ is used, and in the last row, the fact that $\varphi_i^{k+} = 0$ for all $i \notin \mathcal{V}_k$ is used. Now, considering that $[\mathbf{C}(\mathbf{u})]_{ii}$ has a $(1, 1)$ -th zero element, i.e., $[C_{11}(t, \Phi\bar{\mathbf{u}})]_{ii} = 0$, and that if $k \neq l$ then $i \notin \mathcal{V}_l$ and thus $\varphi_i^l = \mathbf{0}$, it follows that for some index $i \in \mathcal{V}_k$,

$$\varphi_i^{k+} [\mathbf{C}(t, \Phi\bar{\mathbf{u}})]_{ii} \varphi_i^l = \varphi_i^{k+} [\mathbf{C}(t, \Phi\bar{\mathbf{u}})]_{ii} \varphi_i^k = \frac{|E_i|}{|\Omega_k|} [C_{11}(t, \Phi\bar{\mathbf{u}})]_{ii} = 0 \quad (49)$$

The matrix $[\Phi^+ \mathbf{C}(t, \Phi\bar{\mathbf{u}}) \Phi]_{kl} = 0$ for all $k, l = 1, 2, \dots, N$, and thus,

$$\bar{\mathbf{C}}(t, \bar{\mathbf{u}}) = \Phi^+ \mathbf{C}(t, \Phi\bar{\mathbf{u}}) \Phi = \mathbf{0} \quad (50)$$

as indicated by the LCM in eq. (8).

A.2.2 Magnitude Analysis for Residual Dynamics

Next, the magnitude of the residual dynamics $\mathbf{r}^{(2)}(\mathbf{u}, t)$ is analyzed to pinpoint the missing physics in the LCM. By definition,

$$\mathbf{r}^{(2)}(\mathbf{u}, t) = \dot{\bar{\mathbf{u}}} - \mathbf{r}^{(1)}(\bar{\mathbf{u}}, t) \quad (51a)$$

$$= \Phi^+ \mathbf{r}(\mathbf{u}, t) - \mathbf{r}^{(1)}(\mathbf{u}, t) \quad (51b)$$

$$\begin{aligned} &= \underbrace{\Phi^+ \mathbf{A}(\mathbf{u})^{-1} \mathbf{B}(\mathbf{u}) \mathbf{u} - \bar{\mathbf{A}}(\bar{\mathbf{u}})^{-1} \bar{\mathbf{B}}(\bar{\mathbf{u}}) \bar{\mathbf{u}}}_{\#1} + \underbrace{\Phi^+ \mathbf{A}(\mathbf{u})^{-1} \mathbf{C}(\mathbf{u}) \mathbf{u} - \bar{\mathbf{A}}(\bar{\mathbf{u}})^{-1} \bar{\mathbf{C}}(t, \bar{\mathbf{u}}) \bar{\mathbf{u}}}_{\#2} \\ &\quad + \underbrace{\Phi^+ \mathbf{A}(\mathbf{u})^{-1} \mathbf{f}(t) - \bar{\mathbf{A}}(\bar{\mathbf{u}})^{-1} \bar{\mathbf{f}}(t)}_{\#3} \end{aligned} \quad (51c)$$

The magnitude analysis for terms $\#1$ and $\#3$ can be found in Ref. [x](#). The analysis for term $\#2$ is presented next. Let $\mathbf{D}(\bar{\mathbf{u}}) = \mathbf{A}(\Phi\bar{\mathbf{u}})^{-1} \mathbf{P} \mathbf{C}(t, \Phi\bar{\mathbf{u}})$, then,

$$\Phi^+ \mathbf{A}(\mathbf{u})^{-1} \mathbf{C}(\mathbf{u}) \mathbf{u} - \bar{\mathbf{A}}(\bar{\mathbf{u}})^{-1} \bar{\mathbf{C}}(t, \bar{\mathbf{u}}) \bar{\mathbf{u}} \quad (52a)$$

$$= \Phi^+ \mathbf{A}(\mathbf{u})^{-1} \mathbf{C}(\mathbf{u}) \mathbf{u} - \Phi^+ \mathbf{A}(\Phi\bar{\mathbf{u}})^{-1} \mathbf{P} \mathbf{C}(t, \Phi\bar{\mathbf{u}}) \Phi \Phi^+ \mathbf{u} \quad (52b)$$

$$= \Phi^+ \mathbf{A}^{-1}(\mathbf{u}) \mathbf{C}(\mathbf{u}) \mathbf{u} - \Phi^+ \mathbf{D}(\bar{\mathbf{u}}) \Phi \Phi^+ \mathbf{u} \quad (52c)$$

$$(52d)$$

367 where $\mathbf{P} = \Phi\Phi^+$. Thus,

$$\|\Phi^+\mathbf{A}(\mathbf{u})^{-1}\mathbf{C}(\mathbf{u})\mathbf{u} - \bar{\mathbf{A}}^{-1}(\bar{\mathbf{u}})\bar{\mathbf{C}}(t, \bar{\mathbf{u}})\bar{\mathbf{u}}\| \quad (53a)$$

$$\leq \|\Phi^+\mathbf{A}^{-1}(\mathbf{u})\mathbf{C}(\mathbf{u})\mathbf{u} - \Phi^+\mathbf{D}(\bar{\mathbf{u}})\mathbf{u}\| + \|\Phi^+\mathbf{D}(\bar{\mathbf{u}})\mathbf{u} - \Phi^+\mathbf{D}(\bar{\mathbf{u}})\Phi\Phi^+\mathbf{u}\| \quad (53b)$$

$$\leq \|\Phi^+\| \underbrace{\|\mathbf{A}^{-1}(\mathbf{u})\mathbf{C}(\mathbf{u})\mathbf{u} - \mathbf{D}(\bar{\mathbf{u}})\mathbf{u}\|}_{\#1} + \|\Phi^+\mathbf{D}(\bar{\mathbf{u}})\| \underbrace{\|\mathbf{u} - \Phi\Phi^+\mathbf{u}\|}_{\#2} \quad (53c)$$

368 where term $\#2$ is due to the appriximation of non-uniform temperaeture as constants, and
369 term $\#1$ is the error in the advection dynamics due to coarse-graining.

370 A.3 Lumped Capacitance Model

371 The following assumptions are employed: (1) the temperature in component (i) is described
372 by a scalar time-varying average temperature $\bar{u}^{(i)}$, (2) between neighboring components (i)
373 and (j) the heat flux is approximated as,

$$q_{ij} = \frac{\bar{u}^{(j)} - \bar{u}^{(i)}}{R_{ij}} \quad (54)$$

374 where R_{ij} is the thermal resistance. Empirically, for a component of isotropic heat conduc-
375 tivity k , length ℓ , and cross-section area A , the thermal resistance is $R = \ell/kA$. Between
376 components i and j , define $R_{ij} = R_i + R_j$. In addition, the heat flux due to Dirichlet
377 boundary condition is computed as $q_{iT} = (T_b - \bar{u}^{(i)})/R_i$.

378 At component i , the dynamics of LCM are given by,

$$\int_{E^{(i)}} \rho c_p \dot{\bar{u}}^{(i)} dE^{(i)} = \left(\sum_{j \in \mathcal{N}_i} \int_{e_{ij}} \frac{\bar{u}^{(j)} - \bar{u}^{(i)}}{R_{ij}} de_{ij} \right) + \int_{e_{iq}} q_b de_{iq} + \int_{e_{iT}} \frac{T_b - \bar{u}^{(i)}}{R_i} de_{iT} \quad (55a)$$

$$\bar{A}^{(i)} \dot{\bar{u}}^{(i)} = \left(\sum_{j \in \mathcal{N}_i} \frac{|e_{ij}|}{R_{ij}} (\bar{u}^{(j)} - \bar{u}^{(i)}) \right) + |e_{iq}| \bar{q}^{(i)} + \frac{|e_{iT}|}{R_i} (\bar{T}^{(i)} - \bar{u}^{(i)}) \quad (55b)$$

$$= \sum_{j \in \mathcal{N}_i} \left(-\frac{|e_{ij}|}{R_{ij}} \bar{u}^{(i)} + \frac{|e_{ij}|}{R_{ij}} \bar{u}^{(j)} \right) + \left(-\frac{|e_{iT}|}{R_i} \bar{u}^{(i)} \right) + \left(|e_{iq}| \bar{q}^{(i)} + \frac{|e_{iT}|}{R_i} \bar{T}^{(i)} \right) \quad (55c)$$

$$= \sum_{j \in \mathcal{N}_i \cup \{T_b\}} \left(\bar{B}_{ij}^{(i)} \bar{u}^{(i)} + \bar{B}_{ij}^{(j)} \bar{u}^{(j)} \right) + \bar{f}^{(i)} \quad (55d)$$

379 where in eq. (55b) $|e|$ denotes the length ($d = 2$) or area ($d = 3$) of a component boundary
380 e . The $\bar{A}^{(i)}$, $\bar{B}_{ij}^{(i)}$, and $\bar{B}_{ij}^{(j)}$ quantities are provided in eq. (11).

381 The lumped-mass representation for the four-component TPS is shown in Fig. 2. Let v_i

³⁸² represent the area of the i -th element, $\overline{\rho c_p}_i$, the heat capacity evaluated using the average
³⁸³ temperature $\bar{u}^{(i)}$, and $1/R_{ij} = 1/R_i(\bar{u}^{(i)}) + 1/R_j(\bar{u}^{(j)})$ the equivalent thermal resistance
³⁸⁴ between elements i and j . Leveraging the formulas from eqs. (10) and (11), the LCM
³⁸⁵ matrices are given by,

$$\bar{\mathbf{A}} = \begin{bmatrix} \overline{\rho c_p}_1 v_1 & 0 & 0 & 0 \\ 0 & \overline{\rho c_p}_2 v_2 & 0 & 0 \\ 0 & 0 & \overline{\rho c_p}_3 v_3 & 0 \\ 0 & 0 & 0 & \overline{\rho c_p}_4 v_4 \end{bmatrix}, \quad (56a)$$

$$\bar{\mathbf{B}} = \begin{bmatrix} \frac{1}{R_{12}} + \frac{1}{R_{14}} & -\frac{1}{R_{12}} & 0 & -\frac{1}{R_{14}} \\ -\frac{1}{R_{12}} & \frac{1}{R_{12}} + \frac{1}{R_{24}} + \frac{1}{R_{23}} & -\frac{1}{R_{23}} & -\frac{1}{R_{24}} \\ 0 & -\frac{1}{R_{32}} & \frac{1}{R_{32}} + \frac{1}{R_{34}} & -\frac{1}{R_{34}} \\ -\frac{1}{R_{14}} & -\frac{1}{R_{24}} & -\frac{1}{R_{34}} & \frac{1}{R_{14}} + \frac{1}{R_{24}} + \frac{1}{R_{34}} \end{bmatrix}, \quad \bar{\mathbf{f}} = \begin{bmatrix} \bar{q}^{(1)} \\ \bar{q}^{(2)} \\ \bar{q}^{(3)} \\ 0 \end{bmatrix} \quad (56b)$$